



## Fabrication and optical dispersions of three-dimensional hierarchical plasmonic nanostructures



Woo Ri Ko <sup>a,1</sup>, Manpreet Boora <sup>b,1</sup>, Tru Nguyen Dang <sup>a</sup>, Jae Kyeom Kim <sup>a</sup>, Jinlin Zhang <sup>b</sup>, Junghyo Nah <sup>c</sup>, Zhiyong Fan <sup>d</sup>, Jae Yong Suh <sup>b,\*</sup>, Min Hyung Lee <sup>a,\*</sup>

<sup>a</sup> Department of Applied Chemistry, Kyung Hee University, Yongin, Gyeonggi 17104, South Korea

<sup>b</sup> Department of Physics, Michigan Technological University, Houghton, Michigan 49931, USA

<sup>c</sup> Department of Electrical Engineering, Chungnam National University, Daejeon 34134, South Korea

<sup>d</sup> Department of Electronic and Computer Engineering, The Hong Kong University of Science and Technology, Clear Water Bay, Kowloon, Hong Kong Special Administrative Region

### ARTICLE INFO

#### Article history:

Received 28 October 2021

Revised 17 November 2021

Accepted 17 November 2021

Available online 23 November 2021

#### Keywords:

Anodized aluminum oxide

Hierarchical nanopore

Nanopattern

Nanostructures

Plasmonics

Surface plasmon polariton

### ABSTRACT

This paper describes a facile method for the design and fabrication of hierarchical nanopatterns via aluminum anodization with an application for creating plasmonic crystals. Fabrication of highly-ordered anodized aluminum oxide nanopores requires an applied electric potential for anodization, which is typically set to match the pitch of nanoindentations on Al. This study reports a new voltage regime for Al anodization conditions where the process yields satellite pores of various shapes, periodicities, and sizes around the main pores. These new nanopatterned platforms provide an easy route to fabricate hierarchical metal nanostructures whose energy dispersions are shaped by the mode superposition of the surface plasmon polaritons originating from multiple periodic lattices.

© 2021 The Korean Society of Industrial and Engineering Chemistry. Published by Elsevier B.V. All rights reserved.

### Introduction

Anodized aluminum oxides (AAOs) with self-ordered nanopores (NPs) have been widely studied due to the ease with which nanopatterns can be created with tunable spacing and size without the need for a cleanroom facility. In general, NPs can be self-ordered in honeycomb-like arrangements through a two-step anodization process in diluted acid electrolytes. To form steady-state NPs, the field-assisted dissolution at oxide/electrolyte interfaces should be balanced with oxide formation at metal/oxide interfaces and electrostriction stress [1,2]. Therefore, self-organized NP arrays can only be synthesized under specific anodization conditions [3], as the interpore distances ( $D_{int}$ ) critically depend on the acid electrolytes and applied voltage ( $V_{app}$ ); for instance,  $D_{int}$  of  $\sim 65$  nm in sulfuric acid at 25 V [4],  $\sim 100$  nm in oxalic acid at 40 V [4], and  $\sim 500$  nm in phosphoric acid at 195 V [5]. Although  $D_{int}$  is linearly proportional to  $V_{app}$  ( $D_{int} = V_{app} \times 2.5$  nm/V), it is challenging to obtain NPs with  $D_{int}$  larger than 500 nm due to structure breakdown or burning at high voltages [6]. Also, the drawbacks of long anodizing time and

short-range ordering limited by aluminum (Al) domains make it difficult to apply this technique to plasmonic studies requiring perfectly-ordered nanostructures for precise control of surface plasmon resonance based on the Bragg coupling of plasmonic crystals

To overcome the aforementioned shortcomings of the self-ordering methods, an anodization method using pre-patterned Al has been developed. Nanoindentations in Al can be fabricated via several patterning methods, including photolithography or focused ion-beam (FIB) milling, generating long-range ordered NPs with a larger spacing than self-ordering methods. Nanoindentation makes the anodization process easier upon facilitating nucleation of pores at an early stage. This anodization occurs because an electrolyte can readily penetrate through the pre-patterned dimple structure, and the applied electric fields are guided into the pit regions. Therefore, the use of pre-patterned Al can significantly extend the interpore spacing to which hard anodization methods can barely reach [7,8]. However, as pre-defined patterns fix the geometries of NPs, the fabrication of expensive imprinting molds is additionally required to diversify NP structures such as hierarchical NPs.

Several methods have been proposed to achieve varied pattern geometries from the template-guided anodization approach. The  $D_{int}$  of NP arrays reduced to  $1/\sqrt{3}$  of the lattice constant of

\* Corresponding authors.

E-mail addresses: [jsuh@mtu.edu](mailto:jsuh@mtu.edu) (J.Y. Suh), [minhlee@khu.ac.kr](mailto:minhlee@khu.ac.kr) (M.H. Lee).

<sup>1</sup> These authors are equally contributed.

pre-patterns by developing new self-ordered pores under a specific value of  $V_{app}$  [9]. Audrey et al. reported three-dimensional (3D) microtiered NPs formed by stepping down the  $V_{app}$  while driving pore widening between each anodizing step [10]. Wang et al. reported periodic honeycomb NP formations within nanoindentations with a diameter greater than 400 nm [11].

Here, we demonstrate template-guided anodization methods to fabricate NPs with versatile hierarchical geometries. Compared to previous works that use multiple nanoimprints to build hierarchical NPs, our fabrication method generates hierarchical NPs with a single imprint, followed by anodizing Al. Anodization on the imprinted Al can consistently reproduce correct geometries of hierarchical NP structures are reproducibly by controlling  $V_{app}$  and the type of electrolytes. We used these distinctive structures as templates to fabricate plasmonic crystals to confirm the existence of characteristic surface plasmon polariton (SPP) modes from the periodic arrays of primary and satellite NPs.

## Material and methods

### Electropolishing

Aluminum foil (99.999% purity, 2 cm × 1.5 cm in size) with a thickness of 0.3 mm was cleaned in acetone and ethanol. The substrate was electropolished in a mixture of perchloric acid and ethanol with 1:8 ratio by volume under 24 V at approximately 5 °C for 4 min.

### Nano-indentation on Al

All pre-patterns used in this experiment were fabricated by imprinting on polished Al (99.999 %, company, China) using Si molds (Lightsmyth Inc., USA) with nanopillars in hexagonal lattice (500 nm spacing between the centers of two neighboring pores, 200 nm diameter, and 150 nm height) by applying a mechanical pressure of approximately  $2.5 \times 10^4$  N·cm<sup>-2</sup>. The Si mold stamp could be reused 30 to 50 times.

### Anodization of Al

After pre-patterning, anodization was conducted in a low-temperature bath to maintain the low temperatures required for the high voltage. A constant-voltage process was applied at -2 °C~2 °C with stirring for 1 hr. The Al foil was the anode, and the carbon electrode was the cathode. In order to investigate the influence of the electrolyte, we used two primary electrolytes, 0.3 M oxalic acid and 1 wt% phosphoric acid, with variable voltage from 40 V to 160 V.

### Scanning electron microscope (SEM) images

To understand the pore development of AAO NPs with specific anodizing conditions, top- and cross-sectional views of AAO NPs were taken using SEM (FEI model, USA). Before taking cross-sectional SEM images, AAO samples were cut immediately after soaking in liquid N<sub>2</sub> in order to obtain sharply cut edges.

### Plasmonic crystal fabrication

50-nm-thick Au was deposited on hierarchical AAO NPs using a thermal evaporator. Polyurethane (PU, NOA 61, Norland Optical Adhesives) solution was then dropped on the Au layers, and a glass coverslip was cast on the solution. After curing the PU using a UV mercury lamp, the AAOs were etched using phosphoric acid to release Au/PU/glass. To match the refractive index of the Au inter-

faces, the PU was dropped onto the other side of the Au, and a second glass coverslip was added. The Au film with hierarchical NPs was then sandwiched between PU/glass, resulting in a final order of glass/PU/hierarchical Au NP films/PU/glass.

## Results & discussion

### Preparation and characterization of hierarchical AAO nanopores

Fig. 1 describes the construction of versatile, hierarchical AAO NPs using pre-patterned Al foils. Briefly, electropolished Al foils were pre-patterned by imprinting a mold of Si nanopillars of hexagonal arrays. Anodizing pre-patterned Al foils develops hierarchical NPs with an electrical bias smaller than the potential matched to the spacing of the pre-patterns ( $V_{app} = a_0 / 2.5$  nm·V). In addition to the bias-dependent control of hierarchical NPs, the geometries of NPs can also be tuned by changing electrolytes that govern the acidic anion flow into Al<sub>2</sub>O<sub>3</sub>, and thus influencing the electric field, the viscosity of oxide, and material deformation [12]. Oxalic acid can develop ordered triangular NPs in the center of the primary pores. In contrast to oxalic acids, phosphoric acid can produce many satellite pores surrounding the primary pores.

Before constructing hierarchical NPs, we investigated the normal anodizing condition by varying  $V_{app}$  matched with the spacing of pre-patterns on the Al foils [7]. Because the electric field is guided only to the recessed region, the primary pores on anodic oxide formed from the pre-patterned indentation of the Al foil act as the main building blocks for the lattice basis. Then the self-ordered sub-pore units of the secondary lattice construct the hierarchical NP arrays. Fig. S1 shows FE-SEM images of the Al samples before and after the anodization with 200:100:0.5 (v:v:v) DI water: ethylene glycol: phosphoric acid at  $V_{app}$  of 200 V. After imprinting with a Si mold (spacing  $a_0 = 500$  nm, diameter  $d = 165$  nm, and height  $h = 150$  nm) on a polished Al film, the indentations of the hexagonal lattices ( $a_0 = 500$  nm,  $d = 165$  nm, and  $h = 150$  nm) were obtained (Fig. S1a). To develop the pores with the same periodicity as the indentations,  $V_{app}$  was set to 200 V according to the proportionality constant of 2.5 nm/V (2.5 nm/V × 200 V = 500 nm) [13]. After anodization for 1 hour, highly-ordered AAO NPs ( $a_0 = 500$  nm,  $d = 186$  nm, and  $h = 3.5 \mu$  m) were obtained on top of the Al due to the electric fields concentrated at the centers of the indentations (Fig. S1b). Fig. S1c shows the bottom side of the oxide layers after etching the underlying Al. According to the equipfield strength model, the uniform thickness of the oxide layer achieved in the hemispherical shape accounts for the hexagonal unit cells with a scalloped shape [13]. Although a relatively high voltage was applied, the hexagonally close-packed boundary was maintained without any cracking. Straight and vertically long NP channels in the array were observed in the cross-sectional SEM image (Fig. S1d).

Thanks to the non-uniform but periodic electric fields, sub-pores were developed around the primary pores, resulting in the formation of hierarchical nanopatterns. Fig. 2 and Fig. S2 illustrate the FE-SEM images of the hierarchical nanopatterns obtained from the anodization of the same indented Al foils in 1 wt % phosphoric acid while varying  $V_{app}$  from 40 to 160 V. Generally, the 1 wt % phosphoric acid electrolyte is suitable for pre-patterns with intervals of 500 nm [5]. When  $V_{app}$  was set significantly lower than 200 V (as following 2.5 nm/V rules [13]), new pores were developed between pre-patterned pores due to the self-ordering of porous alumina. For example, ~ 57 nm (diameter) sub-NPs with an average spacing of 18 nm developed between the primary pores except for the protective boundary region of circular oxide (*i.e.* oxide regions which prevent field enhanced dissolution for  $D_w = 47$ -nm) next to the primary pore with 40 V anodization (Fig. S2a). As

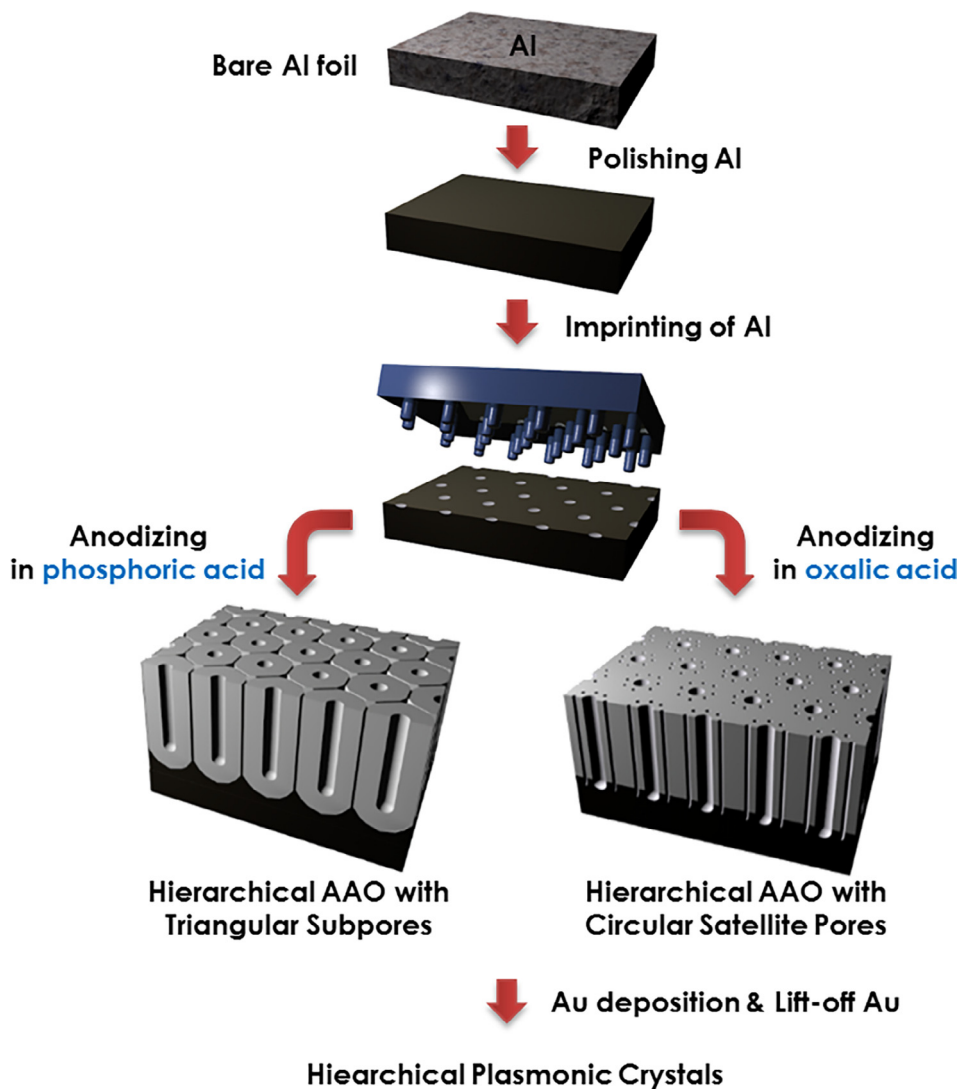


**Fig. 1.** Schematic description of the fabrication steps of hierarchical AAO NPs and the transformation to hierarchical Au plasmonic crystals.

the  $V_{app}$  increased, the diameter of protective oxide boundaries with a spherical shape expanded until they contacted the oxide boundaries of the neighboring pores. When the cylindrical oxide boundaries contacted each other, in contrast, the oxide of the primary pores transformed into a rigid, hexagonal, close-packing structure with the approximate values of  $D_{int} \sim 2.5$  nm/V,  $D_p$  (pore diameter)  $\sim 0.9$  nm/V, and  $D_w \sim 0.8$  nm/V [13–15]. When  $V_{app}$  increased to 100 V, the oxide protective boundary thickness increased ( $D_w = 160$  nm), while the oxide boundary remained in a circular shape due to the insufficient development toward a neighboring oxide. A small bias was required to equal one-half of the voltage of the main pores ( $V_{app} = 100$  V) such that the field-enhanced oxide dissolution occurred at one-half the interdistance between the primary pores (Fig. 2a, b). When  $V_{app}$  was over 120 V, the formation of hexagonal oxide cells were observed (Fig. 2c). Interestingly, small triangular pores with monodisperse size and shape were formed at each corner of the hexagonal cells, as evidenced in the SEM cross-section image (Fig. 2d). At anodizing voltages up to 160 V, the size of the triangular holes decreased as the oxide wall thickened (Fig. S2). The regular hierarchical structures that consist of the ordered primary and surrounding triangular pores were used as templates to create plasmonic crystals supporting surface plasmon polaritons (SPP) [16,17].

The anodization with the same imprinted patterns but various acidic electrolytes can achieve the design flexibility of the hierarchical structures (Fig. 3). By simply changing the electrolyte to 0.3 M oxalic acid, which was previously used to form self-ordered 100-nm-spaced NPs [18], Penrose-type NP structures could be obtained. Similar to the AAO formed in 1 wt% phosphoric acid, randomly distributed pores with a regular  $D_{int}$  of  $\sim 47$  nm were formed around the primary pores when  $V_{app}$  was set to 40 V (Fig. S3a). Unlike the primary pores, these tiny pores did not fully develop in the oxide. However, in 0.3 M oxalic acid, these hierarchical NP structures showed significantly different development trends compared to those formed with phosphoric acid. In the oxalic acid, the oxide protective boundaries (appearing as bright contrast regions around the primary pores) were significantly smaller than those in the phosphoric. When the field-assisted dissolution occurred, the acid facilitated the chemical reaction of oxide dissolution. Also, as the acidity increased, the distance between any two pores became smaller [14]. This high acidity effect of oxalic acid allows the satellite pores to develop further while maintaining the same shape, even under relatively high  $V_{app}$ . With a low  $V_{app}$  (40 to 50 V), the oxide barriers became very thin. As a result, many satellite pores (with a spacing of 13 nm for 40 V and 15 nm for 50 V) were generated between the primary pores,

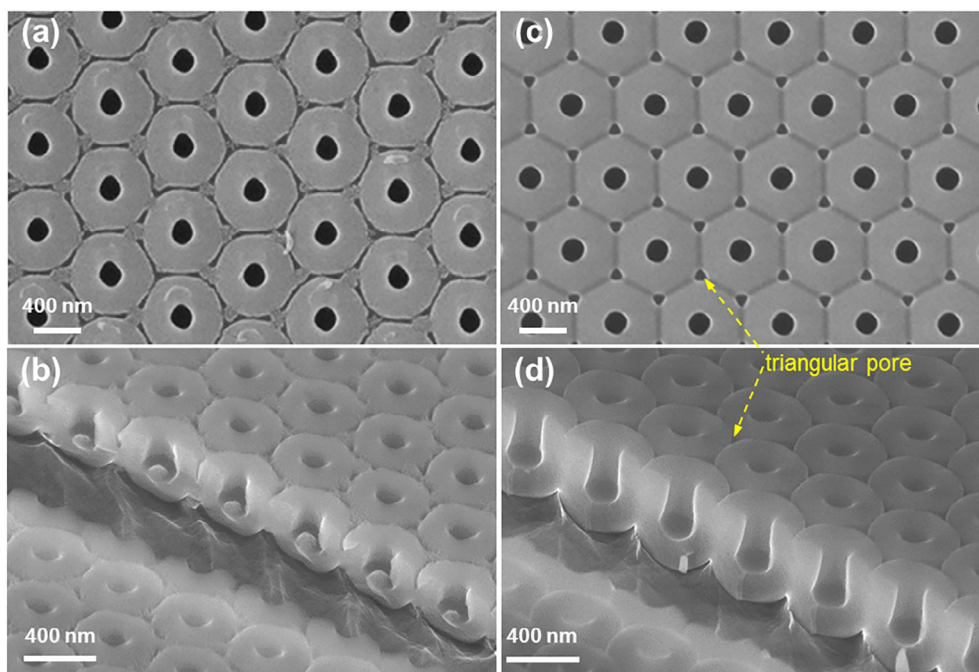


**Fig. 2.** Top-view and cross-sectional-view FE-SEM images of hierarchical NPs fabricated by anodizing at (a, b) 100 V and (c, d) 150 V in 1 wt% phosphoric acid. The arrow indicates triangular sub-pore formation.

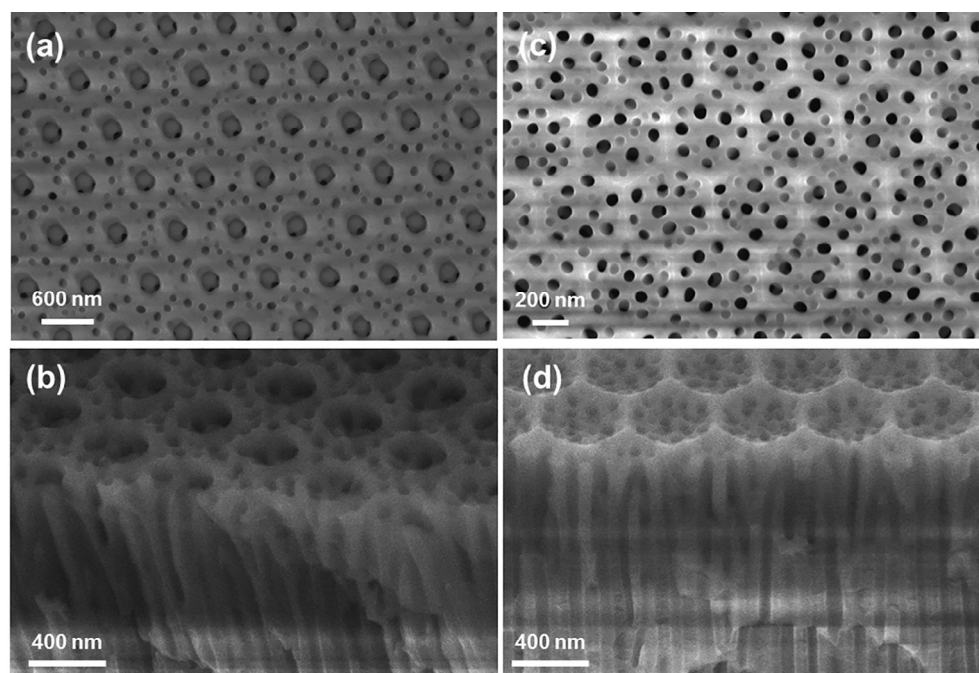


**Fig. 3.** Top-view and cross-section-view FE-SEM images of hierarchical NPs fabricated by anodizing at (a, b) 100 V and (c, d) 150 V in 0.3 M oxalic acid.

where the oxide/metal interface angle ( $\theta_{o/m}$ ) was over  $180^\circ$  (Fig. S3a, b) [19]. When  $V_{app}$  increased to 90 V, the diameter of the protective oxide boundaries increased, and thus the areas of NP nucleation decreased (Fig. S3c, d). Consequently, a smaller number of tiny NPs ( $\sim 43$  nm diameter,  $\sim 131$  nm spacing) were created next to the external edge of the passivated oxide area, with  $\theta_{o/m}$  larger than  $180^\circ$  in the presence of thicker oxide boundary. As the oxide dissolution reached to voltages over 110 V, the circular sub-pores on the oxide boundaries became distinguishable. Typically, circular arrangements of approximately ten satellite pores are formed

around a primary pore. In addition, 2  $\sim$  3 NPs can be observed even in the primary pores at voltages above 110 V (Fig. S3e, f).

Although anodization with  $V_{app} > 150$  V typically causes a structural damage, a new type of NPs in hexagonal cells can be created at this level of applied voltage. At 150 V, hexagonal oxide boundaries developed, as shown in the case with phosphoric acid; however, with a combination of high voltage and an acidic solution, NPs could develop even on the oxide barrier. The pore development process did not continue significantly toward the thicker oxide zone; thus, the hexagonal boundary edge was preserved

(Fig. 3c, d). Previous reports showed that guided anodization using focused-ion-beam (FIB) [7], nano-sphere lithography [11], or nano-stamping [9,19] fabricated hierarchical structures. In contrast, the satellite pores in this study were self-developed via specific anodizing conditions under the acidic electrolytes without the need for additional pre-patterns. We found that the size of the satellite pores followed  $D_{sub} = 0.9 \text{ nm/V}$  under normal anodization conditions, and the size of the primary pores increased linearly with increasing  $V_{app}$ .

The control parameters and their effective ranges for the fabrication of hierarchical structures in this study are summarized in Fig. 4. For the formation of hierarchical AAO in 1 wt% phosphoric acid, selected geometrical features (primary pore diameter, barrier thickness, triangular sub-pore sizes) exhibited characteristic dependences on  $V_{app}$ , as plotted in Fig. 4a. As the applied voltage increased, the primary pore diameter increased from  $\sim 120 \text{ nm}$  to  $200 \text{ nm}$ , and the barrier thickness increased from  $\sim 46 \text{ nm}$  to  $224 \text{ nm}$ . As the barrier grew, the triangular pore size decreased from  $\sim 95 \text{ nm}$  to  $47 \text{ nm}$ . The primary pores of the hierarchical AAO in 0.3 M oxalic acid increased in size from  $112 \text{ nm}$  to  $260 \text{ nm}$  as the voltage increased from  $40 \text{ V}$  to  $140 \text{ V}$ . The size of the satellite pores increased from  $13 \text{ nm}$  to  $141 \text{ nm}$  because the satellite pores promote the dissolution of oxides. (Fig. 4b). When  $V_{app}$  was greater than  $130 \text{ V}$ , the pore sizes of the main and sub-pores increased rapidly, indicating that the dissolution of oxides accelerated at this potential level. Furthermore, the fast dissolution with  $V_{app} > 130 \text{ V}$  was confirmed by the disappearance of the primary pores and the evolution of sub-pores at  $V_{app} = 150 \text{ V}$  (Fig. 3c).

#### Plasmonic properties of hierarchical metallic nanopores

Hierarchical AAO membranes can be used as deposition templates to fabricate hierarchical plasmonic crystal structures (Fig. 5). In this study, we show that the hierarchical plasmonic structures exhibit superposed SPP modes. Hierarchical plasmonic crystals with hexagonal cells were fabricated by depositing 30-nm-thick Au onto the hierarchical AAO samples (Fig. 2c). The Au patterns were successfully transferred onto glass coverslips (refractive index  $n = 1.52$ ) using an optical glue with a refractive index matching that of the glass substrates (see Experimental for detailed fabrication steps). The overall geometrical features are similar to those of the AAO template, except that the shrinkage of the triangular-shaped pores ultimately results in triangular dimples due to the grain size of Au. A hierarchical Au film consisting of

hexagonal Au cells and NP arrays of periodicity  $p = 500 \text{ nm}$  was obtained (Fig. S4). Triangular-shaped NPs are located at the six base vertices of the hexagonal cells, and the main pore of relatively larger size is located at the center of each cell. This hierarchical array also contains the trench grating of a honeycomb lattice, as defined by the grating lines formed in the interfacing region of closely packed nanodomains. The samples show a high uniformity over a sizable patterned area, which allows us to investigate their angle-dependent optical properties.

To understand the SPP characteristics of the fabricated hierarchical plasmonic structures, we investigated the reflection and transmission dispersions of the Au films on hierarchical AAO NPs with satellite sub-pores around the main central pores (Fig. 5 and Fig. S5). The reflection spectra were measured from the samples of periodicity  $p = 600 \text{ nm}$  and  $50 \text{ nm}$  thick Au film on the top surface. The  $50 \text{ nm}$  thickness was chosen to support the long-range SPP modes with a relatively small dissipation. Each reflection spectrum taken with incident angles ranging from  $10^\circ$  to  $60^\circ$  was stacked to produce the reflection dispersion maps. In general, the SPP modes are identified as dark dispersive bands in convex regions of optical transmittance and reflectance, which represent the decrease in their detected intensity. In Fig. S5, a dark band exists between  $650 \text{ nm}$  to  $750 \text{ nm}$  with a dependence on the azimuthal angle. As moving from an azimuthal angle of  $0^\circ$  to  $45^\circ$ , the SPP  $(0, \pm 1)$  and  $(\pm 1, 0)$  modes branches out of the dispersion curves in transmission spectra. In reflection spectra, the major SPP mode exists around  $600 \text{ nm}$  at normal incidence, and the bright  $(-1, 0)$  SPP resonance in reflection corresponds to the dark band in transmission. The hierarchical lattices (hexagonal NPs and honeycomb grating) support the major SPP modes that stem from  $600 \text{ nm}$  at normal incidence as expected from the lattice periodicity. The incident polarization finds the same structure at every  $60^\circ$  of rotation for the hexagonal lattice. In the reflection dispersions with increasing azimuthal angles from  $8^\circ$  (Fig. 5a) to  $37^\circ$  (Fig. 5d), the SPP mode at  $650 \text{ nm}$  exhibits Fano resonances accompanying strong dips (dark mode) that represent light extinction at the SPP wavelengths.

In Fig. 6, the asymmetric line shape can be clearly seen while the double dip in Fano resonance is also present at an incident angle of  $30^\circ$ . The Fano profiles of reflection and transmission spectra result from interfering contributions of resonant (SPP) states and non-resonant states (direct scattering) to the zero diffraction order [20]. The Fano resonances in reflection associated with the SPP modes move according to the SPP-Bragg relation. A strong

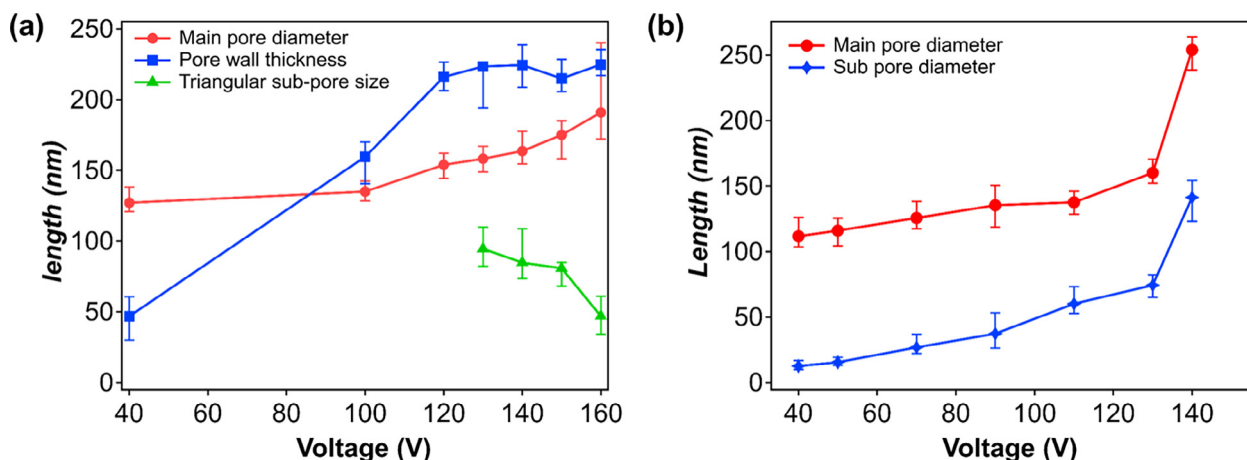
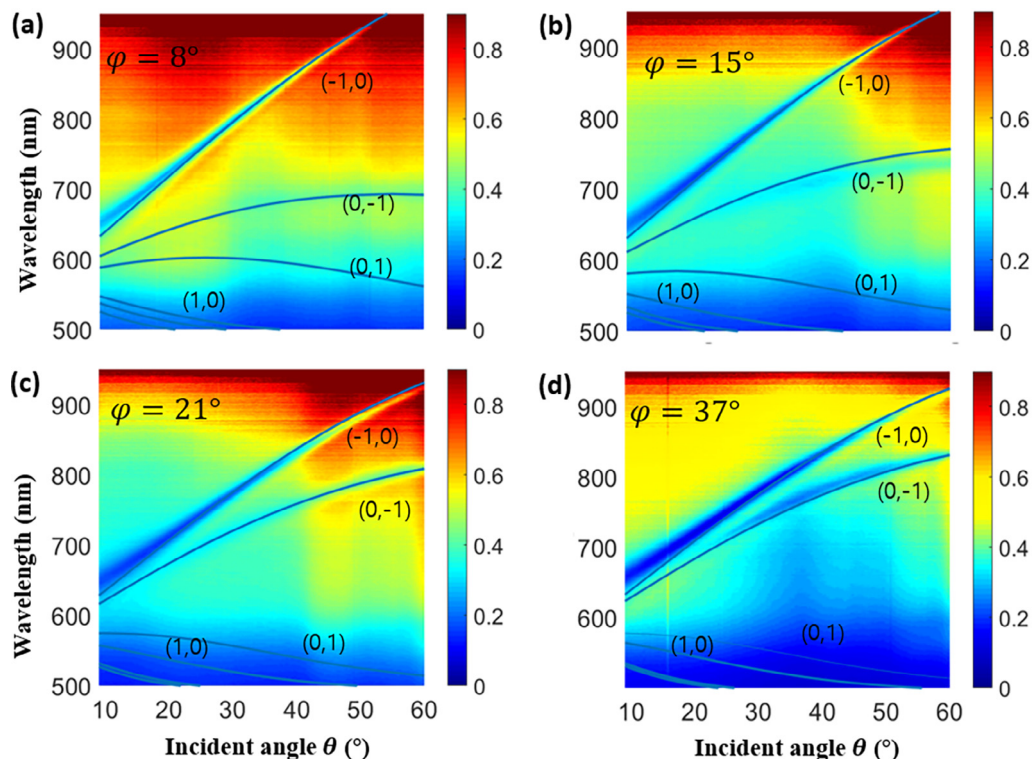


Fig. 4. Dependence of applied voltage on the AAO parameters of (a) main pore diameter, oxide pore wall thickness, and triangular pore size in 1 wt% phosphoric acid and (b) main pore and sub-pore diameter in 0.3 M oxalic acid.



**Fig. 5.** Angle-resolved experimental reflection spectra of hierarchical Au film of 520 nm periodicity and 50 nm thickness for azimuthal angles of (a) 8°, (b) 15°, (c) 21° and (d) 37°. The color bar represents the normalized intensity of the optical transmission. The solid blue curves indicate the SPP modes from the hierarchical hexagonal Au arrays.

transmission band is centered at 600 nm (bright mode). This low-energy SPP mode corresponds only to the hexagonal NP lattice with a low light scattering into high-order transmission paths. Given the lattice structures with *p*-polarized light of incidence, the locations of SPP modes can be calculated using the following SPP-Bragg coupling condition [21],

$$\begin{aligned} |\vec{k}_{spp}| &= \text{Re} \left[ \frac{\omega}{c} \sqrt{\frac{\varepsilon_d \varepsilon_m}{\varepsilon_d + \varepsilon_m}} \right] \\ &= k_0 \sin \theta \cos \phi + k_0 \sin \theta \sin \phi \pm iG_x \pm jG_y \end{aligned} \quad (1)$$

where  $\theta$ ,  $\phi$ ,  $\omega$ ,  $c$ , and  $k_0$  are the incident angle, azimuthal angle, angular frequency, speed, and momentum of free-space light, respectively, and  $G_x$  and  $G_y$  are the magnitudes of the reciprocal lattice vectors for the hexagonal array.  $G_x = \frac{2\pi}{\sqrt{3}a} \hat{x} + \frac{2\pi}{a} \hat{y}$  and  $G_y = -\frac{2\pi}{\sqrt{3}a} \hat{x} + \frac{2\pi}{a} \hat{y}$ , where  $\mathbf{a}$  is the primitive lattice vectors, and  $i$  and  $j$  are the integer orders associated with the mode of the SPP wave vector  $k_{spp}$ .  $\varepsilon_d$  and  $\varepsilon_m$  are the frequency-dependent electric permittivity of the adjacent dielectric media and the metal (Au). The SPP Bragg relation remains the same for both the reflection and transmission spectra. Ordinarily, the minima in the transmission spectra are associated with the maxima in the reflection spectra. The higher-order modes  $(-2,0)$  are visible in the transmission spectra but not in reflection spectra, thus suggesting a much more contribution to the resonances from the diffraction modes from satellite NPs surrounding the central NP. In addition to the SPP characteristics of the fabricated hierarchical plasmonic structures, the transmission and reflection dispersions of the hierarchical Au films from hierarchical AAO NPs with triangular sub-pores (Fig. 2c-d) were also experimentally investigated (Fig. S6 and S7). As calculated from the SPP-Bragg relation, the honeycomb groove lattice also supports the SPP modes that branch out into the  $(\pm 1, 0)$  and  $(0, \pm 1)$  modes with increasing incident angles. In reflection spectra,

at low incident angles between 10° and 30°, a discontinuity in the reflection intensity can be seen in the SPP dispersion curve  $(0, -1)$  for an azimuthal angle of 37°. This feature represents again the interfering effects of SPPs from both the central NPs and the surrounding satellite NPs. No anti-crossing feature is observed in the dispersion, implying that a strong coupling between the two hierarchical lattices does not occur. Compared to the plasmonic structures with a triangular shape, the hexagonal NP lattice supports an SPP mode at 790 nm at normal incidence, clearly visible in the reflection spectrum (Fig. S7). The role of hexagonal NPs in the unit cell can be

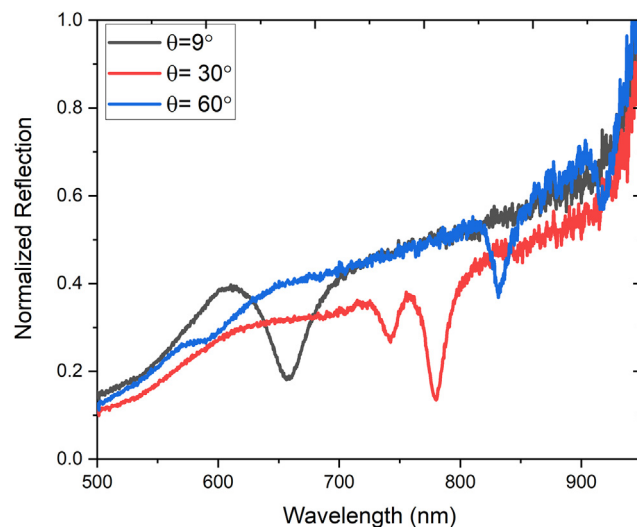


**Fig. 6.** Individual reflection spectrum with an azimuthal angle of 45°. The dip for Fano shape resonance is seen for incident angle 9° and 60°. For incident angle 30° two dips can be seen in spectrum suggesting strong coupling between modes.

further understood from the finite-difference time-domain calculations (Fig. S8). Without the NPs, the honeycomb lattice only supports the SPP modes of small transmission intensity. In the presence of the NPs, the new hexagonal lattice not only adds new SPP modes in the dispersion but also increases substantially the transmission intensity up to 6%. The hexagonal NP lattice is hierarchically higher. It includes the SPP modes from the honeycomb lattice; therefore, the large optical transmission is observed owing to the NPs at the low-energy side of the SPP mode created by the honeycomb grating structure. Hence, the hierarchical structure enhances the Fano-type line shape by supporting both the surface wave propagation and resonant transmission near the SPP wavelengths.

## Conclusion

In summary, we introduce a facile fabrication of hierarchical nanopatterns using template-assisted aluminum anodization. This method provides us with a design flexibility that extends the size of NPs and lattice periodicity beyond conventional anodization methods. Electrolyte composition and anodic voltage critically determine the sample geometries, while this fabrication approach allows the formation of hierarchical patterns consisting of various satellite pore structures around fixed primary pores. Moreover, we demonstrate that these hierarchical AAO patterns can create high-quality hierarchical plasmonic crystals. Complex SPP modes are generated by mixing multiple SPP modes excited on the two lattice parameters of the periodic structures. The SPP modes shows distinct dispersion curves for different shaped NPs. In the applications such as harmonic generators or spectral filters, these 3D plasmonic structures of high-density NPs may have a great advantage in increasing output efficiencies of devices.

## Declaration of Competing Interest

The authors declare that they have no known competing financial interests or personal relationships that could have appeared to influence the work reported in this paper.

## Acknowledgments

This work was financially supported by “Creative Materials Discovery Program” (NRF-2017M3D1A1039379), “Carbon to X Project” (NRF-2020M3H7A1096388), and “the Basic Research Program” (NRF-2021R1A2C2010244) through the National Research Foundation of Korea (NRF) funded by the Ministry of Science and ICT, Republic of Korea.

## Appendix A. Supplementary data

Normal anodizing of imprinted Al films; Hierarchical NPs by anodizing with various biases in 1 wt % phosphoric acid; Hierarchical NPs fabricated via anodization with various biases in 0.3 M oxalic acid; Au hierarchical plasmonic crystals; Transmission dispersion of hierarchical Au with NPs; Transmission dispersion of hierarchical Au with triangular NPs; Reflection dispersion of hierarchical Au with triangular NPs; FDTD calculations. This material can be found at <https://doi.org/10.1016/j.jiec.2021.11.034>.

## References

- [1] T.P. Hoar, N.F. Mott, J. Phys. Chem. Solids 9 (1959) 97–99, [https://doi.org/10.1016/0022-3697\(59\)90199-4](https://doi.org/10.1016/0022-3697(59)90199-4).
- [2] J. Oh, C.V. Thompson, Electrochim. Acta 56 (2011) 4044–4051, <https://doi.org/10.1016/j.electacta.2011.02.002>.
- [3] K. Nielsch, J. Choi, K. Schwirn, R.B. Wehrspohn, U. Gösele, Nano Lett. 2 (2002) 677–680, <https://doi.org/10.1021/nl025537k>.
- [4] A.P. Li, F. Müller, A. Birner, K. Nielsch, U. Gösele, J. Vac. Sci. Technol. 17 (1999) 1428–1431, <https://doi.org/10.1116/1.581832>.
- [5] H. Masuda, K. Yada, A. Osaka, Jpn. J. Appl. Phys. 37 (1998) L1340–L1342, <https://doi.org/10.1143/JJAP.37.L1340>.
- [6] S. Ono, M. Saito, M. Ishiguro, H. Asoh, J. Electrochem. Soc. 151 (2004) B473–B478, <https://doi.org/10.1149/1.1767838>.
- [7] S. Lee, D. Kim, E. Gillette, J. Oh, S.W. Han, S.B. Lee, Phys. Chem. Chem. Phys. 15 (2013) 10659–10665, <https://doi.org/10.1039/C3CP50630D>.
- [8] H. Masuda, H. Asoh, M. Watanabe, K. Nishio, M. Nakao, T. Tamamura, Adv. Mater. 13 (2001) 189–192, doi:10.1002/1521-4095(200102)13:3 <189::AID-ADMA189 3.0.CO;2-Z>
- [9] S. Shingubara, S. Maruo, T. Yamashita, M. Nakao, T. Shimizu, Microelectron. Eng. 87 (2010) 1451–1454, <https://doi.org/10.1016/j.mee.2009.11.112>.
- [10] A.Y.Y. Ho, H. Gao, Y.C. Lam, I. Rodriguez, Adv. Funct. Mater. 18 (2008) 2057–2063, <https://doi.org/10.1002/adfm.200800061>.
- [11] X. Wang, S. Xu, M. Cong, H. Li, Y. Gu, W. Xu, Small 8 (2012) 972–976, <https://doi.org/10.1002/smll.201102274>.
- [12] P. Skeldon, G.E. Thompson, S.J. Garcia-Vergara, L. Iglesias-Rubianes, C.E. Blanco-Pinzon, Electrochem. Solid-State Lett. 9 (2006) B47–B51, <https://doi.org/10.1149/1.2335938>.
- [13] Z. Su, G. Hahner, W. Zhou, J. Mater. Chem. 18 (2008) 5787–5795, <https://doi.org/10.1039/B812432A>.
- [14] G.E. Thompson, Thin Solid Films 297 (1997) 192–201, [https://doi.org/10.1016/S0040-6090\(96\)09440-0](https://doi.org/10.1016/S0040-6090(96)09440-0).
- [15] F. Keller, M.S. Hunter, D.L. Robinson, J. Electrochem. Soc. 100 (1953) 411–419, <https://doi.org/10.1149/1.2781142>.
- [16] M.R. Jones, K.D. Osberg, R.J. Macfarlane, M.R. Langille, C.A. Mirkin, Chem. Rev. 111 (2011) 3736–3827, <https://doi.org/10.1021/cr1004452>.
- [17] D. Shan, L. Huang, X. Li, W. Zhang, J. Wang, L. Cheng, X. Feng, Y. Liu, J. Zhu, Y. Zhang, J. Phys. Chem. C 118 (2014) 23930–23936, <https://doi.org/10.1021/jp5026152>.
- [18] O. Jessensky, F. Müller, U. Gösele, Appl. Phys. Lett. 72 (1998) 1173–1175, <https://doi.org/10.1063/1.121004>.
- [19] J. Choi, R.B. Wehrspohn, U. Gösele, Electrochim. Acta 50 (2005) 2591–2595, <https://doi.org/10.1016/j.electacta.2004.11.004>.
- [20] M. Sarrazin, J.-P. Vigneron, J.-M. Vigoureux, Phys. Rev. B 67 (2003), <https://doi.org/10.1103/PhysRevB.67.085415>.
- [21] W.L. Barnes, W.A. Murray, J. Dintinger, E. Devaux, T.W. Ebbesen, Phys. Rev. Lett. 92 (2004), <https://doi.org/10.1103/PhysRevLett.92.107401>.